I&EC research
Industrial & Engineering Chemistry Research

Article

Cite This: Ind. Eng. Chem. Res. 2018, 57, 11702−11711

pubs.acs.org/IECR

openCrys: Open-Source Software for the Multiscale Modeling of Combined Antisolvent and Cooling Crystallization in Turbulent Flow

Cezar A. da Rosa*,† and Richard D. Braatz‡

†School of Chemistry and Food Science, Federal University of Rio Grande - FURG, Rio Grande - RS, 96203-900, Brazil

‡Department of Chemical Engineering, Massachusetts Institute of Technology - MIT, Cambridge, Massachusetts 02139, United States

Supporting Information

ABSTRACT: The open-source software, called openCrys, is provided for the multiscale simulation of antisolvent and combined antisolvent-cooling crystallization. It simulates the macro- and micromixing scales, and the complete energy and population balance equations during crystal nucleation and growth. The model is based on the Reynolds-Averaged-Navier−Stokes equation, coupled with a three-environment presumed probability density function model, and the spatially varying population balance equation semidiscretized using a high resolution finite-volume method. openCrys is implemented in C++ object oriented programming language using the open-source CFD package OpenFOAM. The software is used to compare the performance of dual impinging jet, coaxial, and radial crystallizers. It is shown that improving the micromixing does not necessarily result in a narrower crystal size distribution when temperature effects are taken into account. The complex interplay of crystallizer kinetics and momentum, mass, and heat transfer makes the selection of the best mixer for a particular application to be nonobvious, which motivates the development and application of high-fidelity multiscale simulations for the design of antisolvent crystallizers.

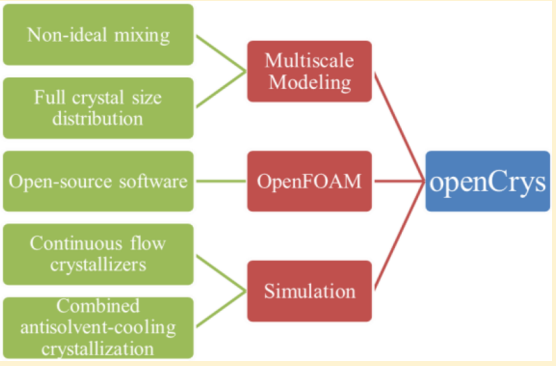

1. INTRODUCTION

Crystallization is a unit operation widely used in the production of high-value chemicals, including pharmaceuticals, catalysts, fragrances, and pigments. Several crystallizer designs and crystallization techniques have been applied by the industry in order to obtain products with desired molecular purity and crystal size distribution (CSD).[1,2]

Among various crystallization methods, especially in the pharmaceutical industry, the antisolvent crystallization technique has the advantage of inducing crystallization of thermally sensitive pharmaceuticals without generating large temperature variations.[3,4] In order to generate higher supersaturation, the antisolvent technique can be combined with cooling crystallization.[5,6] Since these methods require rapid and sufficient mixing of the antisolvent with the solute dissolved in solvent, the design and optimization of such crystallizers play an important role in achieving an effective crystallization with controlled CSD.

Over the past decade, computational fluid dynamics (CFD) has become a well-established tool to simulate, analyze, and design complex flow systems, including micromixers,[7] filtration devices,[8] fast pyrolysis reactors,[9] crystallizers,[10−12] and precipitation reactors.[13−15] These results have demonstrated that a deeper understanding of the phenomena can be obtained that can facilitate the design and optimization of such devices, especially for processes that involve large numbers of particles undergoing chemical reactions and/or physical transformations under complex fluid flow.

The presence of antisolvent in a crystallization generates large spatially localized gradients in supersaturation, which is why nonideal mixing has been especially investigated for this method for inducing crystal nucleation and growth. The dominant flow regime for most antisolvent and combined antisolvent-cooling crystallizers is turbulence, for which a high-fidelity simulation of the key phenomena typically requires mathematical models for mixing at the microscale (micromixing), species transport, the full crystal size distribution, and a complete energy balance. These simulations can be carried out by coupling CFD, micromixing modeling, and population and energy balance equations. Most past studies have implemented coupled CFD, micromixing, and equations for the particle dynamics as user-defined functions in commercial CFD softwares, which then acted as the numerical solver for the multiple particle differential-algebraic equations describing the system.[10,12−15] Some advantages of commercial packages are its wide usage in the chemical industry and its user-friendly interface, whereas some drawbacks are that the user-defined functions limit the ability to introduce complex physics or numerical algorithm modifications, the user-defined functions can break when versions of the software change, a commercial license is required that is especially

Received: May 4, 2018
Revised: July 25, 2018
Accepted: July 25, 2018
Published: July 26, 2018

DOI: 10.1021/acs.iecr.8b01849
Ind. Eng. Chem. Res. 2018, 57, 11702−11711

expensive when running on a large number of processors as required in particle-fluid simulations, and the growth of features has become much slower than for open-source CFD solvers due to the large number of CFD users moving to open source.

OpenFOAM is the most widely used open-source CFD package, which allows anyone to inspect and alter the source codes and hence enables code customization. OpenFOAM is developed based on the fundamental ideas of object orientation, layered software design, and equation mimicking. Many CFD solvers for specialized applications and mesh utilities have been implemented and tested using OpenFOAM as its base, including polydisperse flows,[16] viscoelastic fluid flow,[17] gas–solid flows,[18] and crystallization.[19,20] Especially relevant to chemical engineering applications is its strong capabilities for handling multiphase flows, sharp gradients in heat and mass flows, and particle tracking. Although similar model implementations in OpenFOAM can be found in the literature,[19] neither are they freely available nor do they consider nonlinear mixing effects, such as heat of mixing. To the best of our knowledge there is no publicly available implementation in OpenFOAM for the coupling of CFD macromixing, micromixing, energy balance, and the full population balance equation. Because such a software implementation is not publicly and freely available, research progress and industrial applications of the modeling and simulation of antisolvent and combined antisolvent-cooling have been limited. This article presents such an implementation of these equations in OpenFOAM. The software, openCrys, is available at https://github.com/darosacezar/openCrys.

The software implements a multiscale model, capable of predicting macro- to micromixing scales, as well as the full CSD and energy conservation, including nonideal mixing rules. The software is applied to simulate combined antisolvent-cooling crystallization occurring in turbulent flow (pure antisolvent and pure cooling are special cases). The Reynolds-averaged Navier–Stokes equation with variable properties is coupled with a three-environment presumed probability density function (PDF) micromixing model,[21] the spatially varying population balance equation semidiscretized using a high-resolution finite-volume method, and energy balance and scalar transport equations. The software is used to compare the performance of dual impinging jet, coaxial, and radial crystallizers.

The model equations are followed by a description of the numerical implementation, case studies, results and discussion, and conclusions. More details on the software implementation are provided in the Supporting Information.

2. MODEL EQUATIONS AND OPENFOAM IMPLEMENTATION

This work employs a multiscale mathematical modeling approach. The model couples (1) the dynamic Reynolds-averaged Navier–Stokes equations (RANS) for modeling macromixing with (2) a multienvironment presumed probability density function (PDF) model, which captures the micromixing in the subgrid scale, (3) the spatially varying population balance equation (PBE), which models the evolution of the crystal size distribution, and (4) the energy balance equation to account for the heat transfer between the solvent and antisolvent, as well as the heat of mixing and crystallization.

2.1. Mass and Momentum Conservation. The macromixing was modeled by the Reynolds-averaged Navier–Stokes (RANS) model and the standard k-ε turbulence model with enhanced wall treatment. In general form, the equations are

$$\text{Continuity equation: } \frac{\partial \rho}{\partial t} + \nabla\cdot(\rho\vec{v}) = 0 \tag{1}$$

$$\text{Momentum conservation equation: } \frac{\partial}{\partial t}(\rho\vec{v}) + \nabla\cdot(\rho\vec{v}\vec{v}) = -\nabla p + \nabla\cdot(\bar{\bar{\tau}}) + \rho\vec{g} \tag{2}$$

Standard k-ε equations:

$$\frac{\partial}{\partial t}(\rho k) + \nabla\cdot(\rho k\vec{v}) = \nabla\cdot\left[\left(\mu + \frac{\mu_t}{\sigma_k}\right)\nabla\cdot k\right] + G_k - \rho\varepsilon + S_k$$

$$\frac{\partial}{\partial t}(\rho\varepsilon) + \nabla\cdot(\rho\varepsilon\vec{v}) = \nabla\cdot\left[\left(\mu + \frac{\mu_t}{\sigma_\varepsilon}\right)\nabla\cdot\varepsilon\right] + C_{1\varepsilon}\frac{\varepsilon}{k}G_k - C_{2\varepsilon}\rho\frac{\varepsilon^2}{k} + S_\varepsilon$$

$$\mu_t = \rho C_\mu \frac{k^2}{\varepsilon} \tag{3}$$

Although the model was implemented and tested with the standard k-ε turbulence model, any k-ε turbulence model already implemented in OpenFOAM, as well as model constants, can be chosen via OpenFOAM's user input "turbulenceProperties" dictionary.

In order to account for variable thermodynamic properties such as density, viscosity, heat capacity, and conductivity, which are due to the mixing of the antisolvent with the solvent solution, both ideal and nonideal mixing rules were implemented in OpenFOAM via a new C++ class called twoFluidMixingThermoTransportModel. This class incorporates all the necessary functions to deal with either ideal or nonideal mixing rules, which can be specified via the user input dictionary.

Micromixing was modeled using a three-environment presumed probability density function (PDF) model.[21] One environment is associated with the solute dissolved in solvent, one environment is associated with the added antisolvent, and a third environment is associated with the mixture of solute, solvent, and antisolvent. Scalar transport equations, supplemented with extra terms to deal with micromixing, were used to model species concentration distribution in the third environment. These equations allied with the transport equations for the probabilities of the other two environments (as detailed in the next section) allow the calculation of the mean species concentration and mixture properties in every grid cell of the computational domain.

2.2. Micromixing Model. Following the work of Marchisio et al.,[13−15] Woo et al.,[10,11] and Pirkle Jr. et al.,[12] the micromixing effects were considered by applying the finite-mode presumed probability density function (PDF) model.[21] In this approach, each computational cell in the grid is divided into N_e different probability modes (aka environments), which correspond to a discretization of the presumed composition PDF into a finite set of delta (δ) functions:

$$f_\phi(\boldsymbol{\psi}; \mathbf{x}, t) = \sum_{n=1}^{N_e} p_n(\mathbf{x}, t) \prod_{\alpha=1}^{N_s} \delta[\psi_\alpha - \langle\phi_\alpha\rangle_n(\mathbf{x}, t)] \tag{4}$$

where f_ϕ is the joint PDF of all scalars, N_s is the total number of scalars (species), p_n is the probability of mode n or volume fraction of environment n, and $\langle\phi_\alpha\rangle_n$ is the mean composition

DOI: 10.1021/acs.iecr.8b01849
Ind. Eng. Chem. Res. 2018, 57, 11702−11711

Table 1. Micromixing Terms[21]

Model variables	G, $\mathbf{M}^n$	G_s, $\mathbf{M}_s^n$
p_1	$-\gamma p_1(1-p_1)$	$\gamma_s p_3$
p_2	$-\gamma p_2(1-p_2)$	$\gamma_s p_3$
$\langle \mathbf{s} \rangle_3$	$\gamma[p_1(1-p_1)\langle \boldsymbol{\varphi} \rangle_1 + p_2(1-p_2)\langle \boldsymbol{\varphi} \rangle_2]$	$-\gamma_s p_3(\langle \boldsymbol{\varphi} \rangle_1 + \langle \boldsymbol{\varphi} \rangle_2)$
	$p_3 = 1 - p_1 - p_2$	
	$\gamma = \dfrac{\varepsilon_\xi}{p_1(1-p_1)(1-\langle \xi \rangle_3)^2 + p_2(1-p_2)\langle \xi \rangle_3^2}$	
	$\gamma_s = \dfrac{2D_t}{(1-\langle \xi \rangle_3)^2 + \langle \xi \rangle_3^2} \dfrac{\partial \langle \xi \rangle_3}{\partial x_i} \dfrac{\partial \langle \xi \rangle_3}{\partial x_i}$	
	$\langle \xi'^2 \rangle = p_1(1-p_1) - 2p_1p_3\langle \xi \rangle_3 + p_3(1-p_3)\langle \xi \rangle_3^2$	

of scalar α corresponding to mode n. The weighted concentration is defined as

$$\langle \mathbf{s} \rangle_n \equiv p_n \langle \phi \rangle_n \tag{5}$$

The transport of probability and species in inhomogeneous flow is modeled by

$$\frac{\partial \mathbf{p}}{\partial t} + \sum_i \left[\langle v_i \rangle \frac{\partial \mathbf{p}}{\partial x_i} - \frac{\partial}{\partial x_i}\left(D_t \frac{\partial \mathbf{p}}{\partial x_i} \right) \right] = \mathbf{G}(\mathbf{p}) + \mathbf{G}_\mathbf{s}(\mathbf{p}) \tag{6}$$

$$\frac{\partial \langle \mathbf{s} \rangle_n}{\partial t} + \sum_i \left[\langle v_i \rangle \frac{\partial \langle \mathbf{s} \rangle_n}{\partial x_i} - \frac{\partial}{\partial x_i}\left(D_t \frac{\partial \langle \mathbf{s} \rangle_n}{\partial x_i} \right) \right] = \mathbf{M}^n(\mathbf{p}, \langle \mathbf{s} \rangle_1, ..., \langle \mathbf{s} \rangle_{N_e}) + \mathbf{M}_\mathbf{s}^n(\mathbf{p}, \langle \mathbf{s} \rangle_1, ..., \langle \mathbf{s} \rangle_{N_e}) + p_n \mathbf{S}(\langle \phi \rangle_n) \tag{7}$$

where $\mathbf{G}$ and $\mathbf{M}^n$ are the rates of change of $\mathbf{p} = [p_1, p_2, ..., p_N]$ and $\langle \mathbf{s} \rangle_n$ due to micromixing, respectively, $\mathbf{G}_\mathbf{s}$ and $\mathbf{M}_\mathbf{s}^n$ are additional micromixing terms to eliminate the spurious dissipation rate in the mixture-fraction-variance transport equation (for details see Fox, 2003[21]), and $\mathbf{S}$ is the chemical source term. The conservation of probability requires that

$$\sum_{n=1}^{N} p_n = 1 \tag{8}$$

and

$$\sum_{n=1}^{N_e} G_n(\mathbf{p}) = 0 \tag{9}$$

The mean compositions of the scalars are given by

$$\langle \phi \rangle = \sum_{n=1}^{N_e} p_n \langle \phi \rangle_n = \sum_{n=1}^{N_e} \langle \mathbf{s} \rangle_n \tag{10}$$

and since the means remain unchanged by micromixing,

$$\sum_{n=1}^{N_e} \mathbf{M}^n(\mathbf{p}, \langle \mathbf{s} \rangle_1, ..., \langle s \rangle_{N_e}) = 0 \tag{11}$$

must be satisfied. In this article, a three-environment model was chosen to account for the micromixing effects. In this approach, the solution of solute and solvent is environment 1, the antisolvent represents environment 2, and the mixture of environments 1 and 2 forms environment 3. According to Marchisio et al.,[13−15] the use of three environments is sufficient to capture the micromixing effects in nonpremixed flows with satisfactory accuracy. The micromixing terms for the three-environment model are summarized in Table 1, where the values of $\langle \boldsymbol{\varphi} \rangle_n = \langle \mathbf{s} \rangle_n / p_n$ denote the unweighted variables. For a fully developed scalar spectrum, the scalar dissipation rate, ε_ξ, is related to the turbulent frequency, ε/k, by

$$\varepsilon_\xi = C_\varphi \langle \xi'^2 \rangle \frac{\varepsilon}{k} \tag{12}$$

where $C_\varphi = 2$ [as suggested by Wang and Fox[22]], ε, and k are the turbulent dissipation rate and kinetic energy, respectively, and $\langle \xi'^2 \rangle$ is the mean variance of the mixture fraction $\langle \xi \rangle_3$. By definition, the mixture fractions in environments 1 and 2 are $\langle \xi \rangle_1 = 1$ and $\langle \xi \rangle_2 = 0$, respectively.

The three-environment finite-mode PDF model was implemented in OpenFOAM in a general form through a new C++ class called Foam::PDFModel, where the transport equations of the probabilities of the environments and the weighted mixture fraction are discretized and solved. This class also includes member functions to provide source terms for species transport due to micromixing, population, and energy balance equations, and to calculate the mean properties between the environments and to access the variables of the PDF model. The PDF model equations were discretized with the class fvScalarMatrix (more information on the software implementation is provided in the Supporting Information). A new user input dictionary, PDFdict, was created to specify all the necessary constants for solving the micromixing model equations.

In order to avoid potential undetermined values while calculating γ, analytical expressions were derived using L'Hôpital's rule for the conditions: $\langle \xi \rangle_3 \to 0$; $\langle \xi \rangle_3 \to 1$; $p_1 \to 1$; $p_2 \to 1$; $p_3 \to 1$. Also, to improve numerical stability, especially at the beginning of the numerical solution, a tolerance variable, specified via PDFdict, was introduced for the probability of Environment 3 (p_3). This tolerance represents the smallest value of p_3 considered for calculation purposes. In all the simulations presented in this article, this value was set to 1×10^{-6}.

2.3. Population Balance. The spatially inhomogeneous crystallization is modeled by a population balance equation (PBE, e.g., Randolph and Larson[23]),

$$\frac{\partial f}{\partial t} + \sum_i^N \frac{\partial [G_i(r_i, c, T) f]}{\partial r_i} + \sum_j^3 \left\{ \frac{\partial [v_j f]}{\partial x_j} - \frac{\partial}{\partial x_j}\left[D_t \frac{\partial f}{\partial x_j} \right] \right\} = B(f, c, T) \prod_i \delta(r_i - r_{i0}) + h(f, c, T) \tag{13}$$

where the rates of growth (G_i) and nucleation (B) are functions of the vector of solution concentrations (c) and the

DOI: 10.1021/acs.iecr.8b01849
Ind. Eng. Chem. Res. 2018, 57, 11702−11711

temperature (T), δ is the Dirac delta function, and h describes the creation and destruction of crystals due to aggregation, agglomeration, and breakage. For size-dependent growth, the rate of growth G_i also varies with r_i. This equation is a continuity statement expressed in terms of the particle number density function (f), which is a function of external coordinates (e.g., X, Y, and Z for 3D Cartesian coordinates), internal coordinates (r_i) (e.g., the size dimensions of the crystal), and time (t).

The PBE, discretized along the crystal growth axis using a high-resolution finite volume method,[10,24] was rewritten on a mass basis and solved as a set of scalar transport equations in OpenFOAM, as

$$f_{w,j} = \rho_c k_v \int_{r_{j-1/2}}^{r_{j+1/2}} r^3 f_j \, \mathrm{d}r = \frac{\rho_c k_v f_j}{4}((r_{j+1/2})^4 - (r_{j-1/2})^4) \tag{14}$$

$$\frac{\partial}{\partial t} f_{w,j} + \sum_i^3 \left\{ \frac{\partial [v_i f_{w,j}]}{\partial x_i} - \frac{\partial}{\partial x_i}\left[D_i \frac{\partial f_{w,j}}{\partial x_i} \right] \right\} = \begin{cases} \frac{\rho_c k_v}{4\Delta r}\left[(r_{j+1/2})^4 - (r_{j-1/2})^4\right]\left\{ -G_{j+1/2}\left[f_j + \frac{\Delta r}{2}(f_r)_j \right] + G_{j-1/2}\left[f_{j-1} + \frac{\Delta r}{2}(f_r)_{j-1} \right] + \underbrace{B}_{j=0} \right\}, & \Delta c > 0 \\ \frac{\rho_c k_v}{4\Delta r}\left[(r_{j+1/2})^4 - (r_{j-1/2})^4\right]\left\{ -G_{j+1/2}\left[f_{j+1} - \frac{\Delta r}{2}(f_r)_{j+1} \right] + G_{j-1/2}\left[f_j - \frac{\Delta r}{2}(f_r)_j \right] \right\}, & \Delta c < 0 \end{cases} \tag{15}$$

where $f_{w,j}$ is the cell-averaged crystal mass with units of kg/m^3, $\Delta r = r_{j+1/2} - r_{j-1/2}$ is the discretization for the internal coordinate (e.g., a growth axis), ρ_c is the crystal density, k_v is the crystal volume shape factor, $(f_r)_j$ is the derivative approximated by the minmod limiter,[24] Δc is the supersaturation, and $\underbrace{B}_{j=0}$ is equal to the nucleation rate for the $j = 0$ cell and is equal to zero otherwise. More information on the software implementation is provided in the Supporting Information.

2.4. Energy Conservation. The energy balance assumes that the three environments are in thermal equilibrium at the cell level. Also, compressibility effects were neglected since the fluids are in the liquid phase. Thus, the general form of the energy equation can be written as

$$\frac{\partial}{\partial}(\rho E) + \nabla\cdot[\vec{v}(\rho E + p)] = \nabla\cdot\left[k_{eff}\nabla T + \left(\overline{\overline{\tau}}_{eff}\cdot\vec{v}\right)\right] + S_h$$
$$E + h - \frac{p}{\rho} + \frac{v^2}{2} \tag{16}$$

where k_{eff} is the effective conductivity. The source term (S_h) accounts for the heat of crystallization and heat of mixing between solvent and antisolvent in environment 3, as shown in

$$S_h = S_3(-\Delta H_{mix}) + \left(\sum_j S_{f_{w,j}}\right)(-\Delta H_{crys}) \tag{17}$$

where S_3 is the rate of increase in the concentration of solvent + antisolvent in environment 3, $(\sum_j S_{fw,j})$ is the rate of increase in total crystal mass in environment 3, ΔH_{mix} is the heat of mixing between the solvent and antisolvent in mass basis, and ΔH_{crys} is the heat of crystallization of solute from a solvent/antisolvent mixture in mass basis. The software implementation of the energy balance is described in the Supporting Information

3. NUMERICAL SOLUTION PROCEDURE

This section describes the numerical solution procedure for each equation in turn, in the same order as presented in section 2.

3.1. Discretization of the Momentum Balance Equation. The merged PISO-SIMPLE (PIMPLE) algorithm was applied to run the simulations. This algorithm combines the SIMPLE algorithm with use of the pressure implicit with splitting the operators (PISO) algorithm to rectify the second pressure correction and correct both velocities and pressure explicitly.[25] To explicitly consider the buoyance term, the modified pressure (p_{rgh}) is introduced in

$$p_{rgh} = p - \rho\vec{g}\cdot\vec{x} \tag{18}$$

$$\nabla p = \nabla p_{rgh} + \rho\vec{g} + \vec{g}\cdot\vec{x}\nabla\rho \tag{19}$$

which inserted into the momentum balance equation (eq 2) gives

$$\frac{\partial}{\partial t}(\rho\vec{v}) + \nabla\cdot(\rho\vec{v}\vec{v}) = -\nabla p_{rgh} + \nabla\cdot(\overline{\overline{\tau}}) - \vec{g}\cdot\vec{x}\nabla\rho \tag{20}$$

where $\vec{x}$ is the cell center position vector. The semidiscrete form of this equation used in the merged PIMPLE fluid dynamic solver algorithm can be written as[26]

$$A\vec{v} = H - \nabla p_{rgh} - \vec{g}\cdot\vec{x}\nabla\rho \tag{21}$$

where A represents the diagonal coefficients of the velocity matrix and H consists of the off-diagonal and source terms apart from the pressure gradient. Isolating $\vec{v}$ in this equation gives the velocity predictor equation

$$\vec{v} = A^{-1}H - A^{-1}\vec{g}\cdot\vec{x}\nabla\rho - A^{-1}\nabla p_{rgh} \tag{22}$$

3.2. Pressure and Velocity Correction Equations. The pressure equation is obtained by imposing the volumetric conservation

$$\nabla\cdot\varphi = 0 \tag{23}$$

where φ is the face flux, which is defined by interpolating eq 22 on cell faces and calculating the dot product with the surface normal vector $\vec{S}$:

$$\varphi = (A^{-1}H)_f\cdot\vec{S} - (A^{-1}\vec{g}\cdot\vec{x})_f|\vec{S}|\nabla^{\perp}\rho - A_f^{-1}|\vec{S}|\nabla^{\perp}p_{rgh} \tag{24}$$

Inserting this equation into eq 23 and rearranging the terms gives the pressure equation

$$\nabla\cdot(A_f^{-1}|\vec{S}|\nabla^{\perp}p_{rgh}) = \nabla\cdot\varphi^0 \tag{25}$$

where φ^0 is velocity flux without the contribution of the pressure gradient,

$$\varphi^0 = (A^{-1}H)_f\cdot\vec{S} - (A^{-1}\vec{g}\cdot\vec{x})_f|\vec{S}|\nabla^{\perp}\rho \tag{26}$$

Once the pressure equation (eq 25) is solved, the velocity flux is corrected by

$$\varphi = \varphi^0 - A_f^{-1}|\vec{S}|\nabla^{\perp}p_{rgh} \tag{27}$$

and the velocity is corrected according to

$$\vec{v} = A^{-1}H - A^{-1}rec[(\vec{g}\cdot\vec{x})_f|\vec{S}|\nabla^{\perp}\rho + |\vec{S}|\nabla^{\perp}p_{rgh}] \tag{28}$$

where $rec[(\vec{g}\cdot\vec{x})_f|\vec{S}|\nabla^{\perp}\rho + |\vec{S}|\nabla^{\perp}p_{rgh}]$ is the cell-centered reconstruction of the buoyance and pressure contributions in eq 22 based on the face flux contribution of these terms, which according to Passalacqua and Fox[27] ensures the consistency of the correction with the cell-centered velocities.

DOI: 10.1021/acs.iecr.8b01849
Ind. Eng. Chem. Res. 2018, 57, 11702−11711

3.3. Model Implementation and Solution Procedure.

The model equations were implemented on OpenFOAM 5.0 via the object-oriented C++ programming language. The transport, PBE, and finite-mode PDF properties and variables are input via a set of dictionaries as described in the Supporting Information. The iterative numerical algorithm used to solve all of the model equations is summarized in Figure 1. The discretization schemes implemented for the convection divergence and diffusion (Laplacian) terms were the bounded second-order linear upwind and the unbounded second-order linear-limited differencing schemes, respectively. Grid-independent numerical solutions are obtained by comparing the steady-state solution for different grid sizes.

Initialize simulation data
WHILE time < endTime **DO**
- PIMPLE **DO**
  1. Update fluid mixture properties
  2. Solve momentum equation to obtain the predicted velocities
  3. Solve scalar transport equations
  4. Solve PDF model equations
  5. Solve energy conservation equation
  6. Solve semi-discrete PBEs
  - PISO **DO**
    1. Calculate face flux without the pressure gradient contribution (Eq. 29)
    2. Solve pressure equation (Eq. 28)
    3. Correct face flux (Eq. 30)
    4. Correct cell-centered velocities (Eq. 31)
  - **LOOP**
- **LOOP**
1. Solve turbulence model equations
2. Update PDF model parameters

LOOP

Figure 1. Numerical solution iterative algorithm.

4. CASE STUDIES

This section illustrates the application of the software to the combined antisolvent-cooling crystallization of lovastatin with methanol as solvent and water as antisolvent for dual impinging jet, coaxial, and radial crystallizers (Figure 2). The radial mixer configuration has two inlets of the same diameter and mass flow rate directly across from each other, as that configuration minimizes the potential for fouling.[20] 3D computational domains with $YZl_{x=0}$ plane of symmetry were generated for each geometry. In all of the domains, the diameter of the main pipe was 0.0363 m. The solution(solvent + solute)/antisolvent mass flow ratio was set to 1 in all simulations. Two different total inlet mass flow rates (solution + antisolvent), 0.264 and 1.06 kg/s, were simulated to compare the crystallizers' performances. The inlet temperatures of the solvent and antisolvent streams were set to 305 and 293 K, respectively.

The solubility, nucleation, and growth rates were calculated using[11,28]

$$c^*(\text{kg/kg of solvents}) = 0.001 \exp\left(15.45763\left(1-1/\theta\right)\right)$$
$$\begin{Bmatrix} -2.7455\times10^{-4}W_{as}^3 + 3.3716\times10^{-2}W_{as}^2 - 1.6704W_{as} + 33.089, & \text{for } W_{as} \le 45.67 \\ -1.7884\times10^{-2}W_{as} + 1.7888, & \text{for } W_{as} > 45.67 \end{Bmatrix} \quad (29)$$
$$\theta = \frac{T}{T_{ref}}, \quad T_{ref} = 296\ \text{K}$$

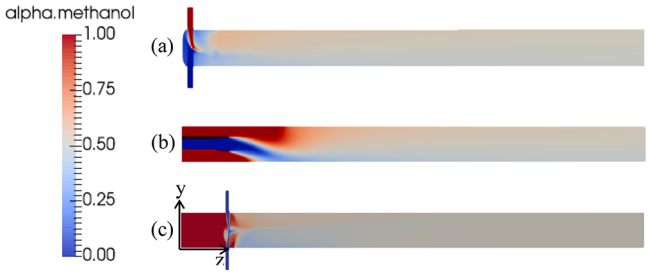

Figure 3. Volume fraction of methanol for a total mass flow rate of 0.264 kg/s: (a) dual impinging jet; (b) coaxial crystallizer; (c) radial crystallizer.

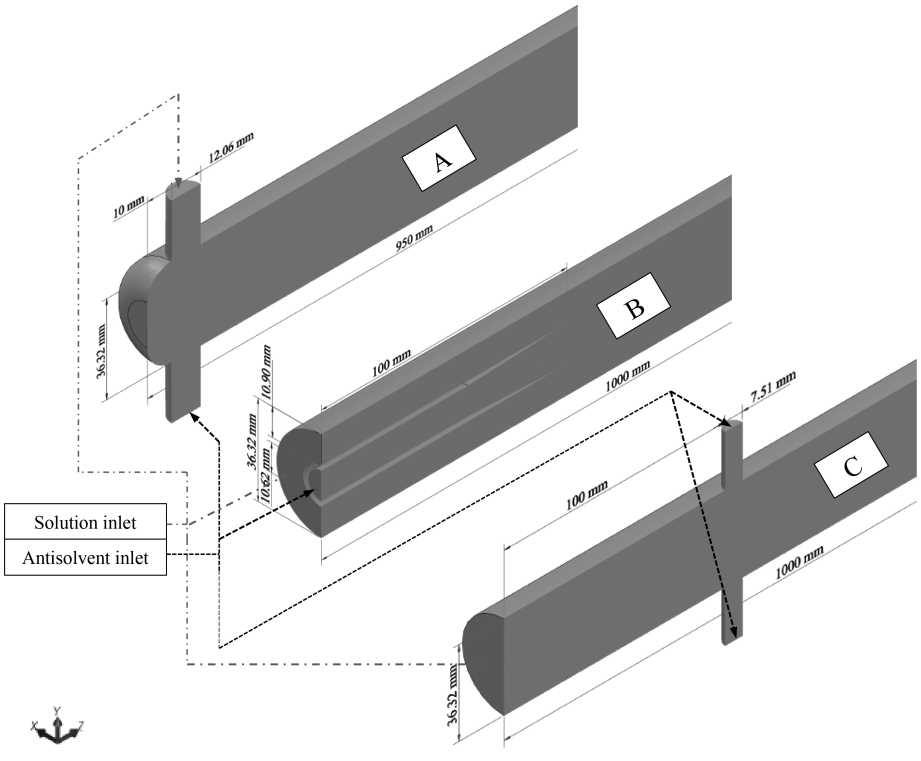

Figure 2. Computational domains used in the simulations: (A) dual impinging jet; (B) coaxial crystallizer; (C) radial crystallizer.

DOI: 10.1021/acs.iecr.8b01849
Ind. Eng. Chem. Res. 2018, 57, 11702−11711

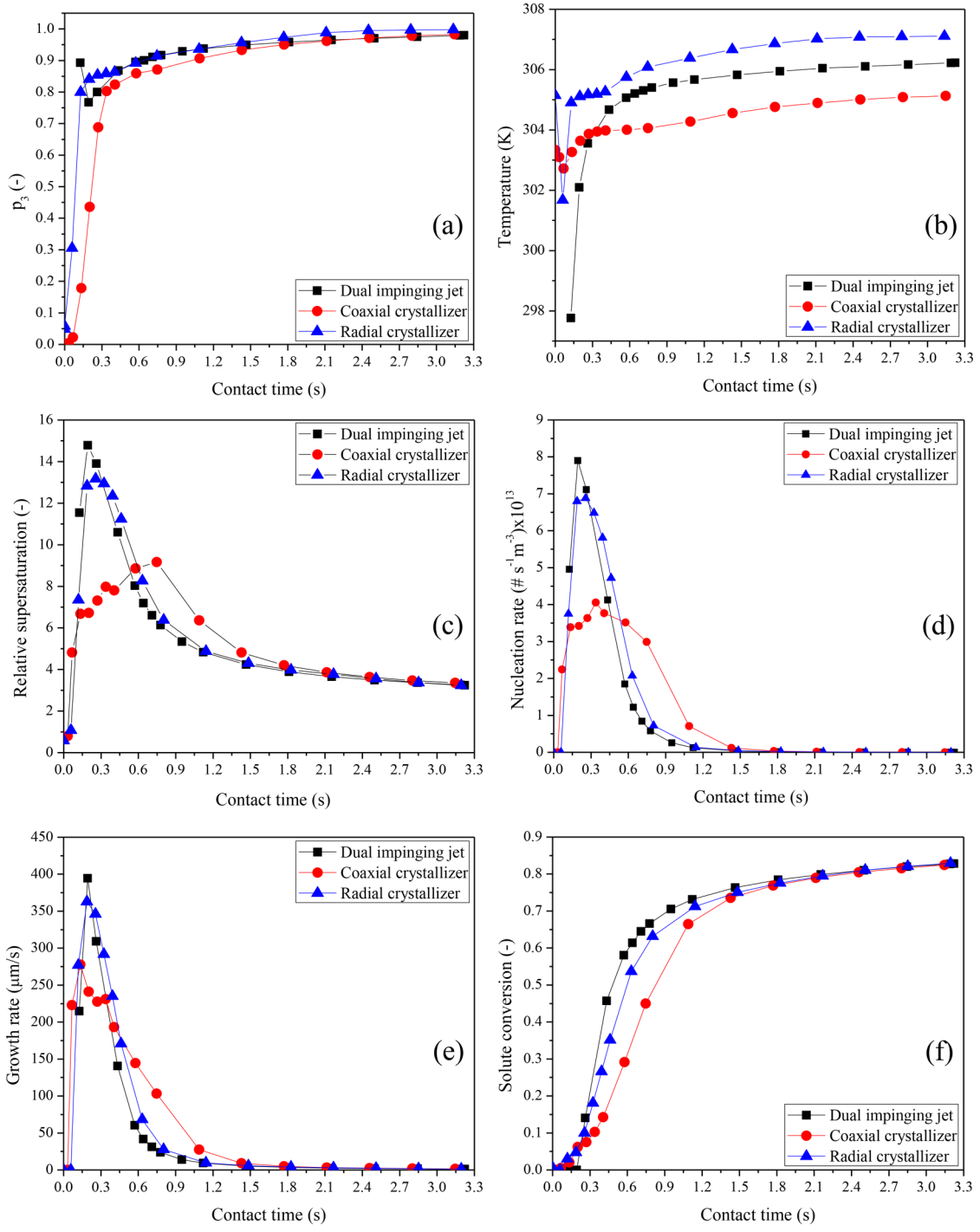

Figure 4. Mass-weighted average variables as a function of contact time calculated for a total mass flow rate of 0.264 kg/s: (a) volume fraction of the mixed environment; (b) temperature; (c) relative supersaturation; (d) nucleation rate; (e) growth rate; (f) solute conversion.

$$B = B_{\text{homogeneous}} + B_{\text{heterogeneous}}$$

$$B_{\text{homogeneous}} \text{ at } 23\,^{\circ}\text{C } (\#/\text{s}\cdot\text{m}^3) = 6.97 \times 10^{14} \exp\left(\frac{-15.8}{[\ln S]^2}\right)$$

$$B_{\text{heterogeneous}} \text{ at } 23\,^{\circ}\text{C } (\#/\text{s}\cdot\text{m}^3) = 2.18 \times 10^{8} \exp\left(\frac{-0.994}{[\ln S]^2}\right) \quad (30)$$

$$G \text{ at } 23\,^{\circ}\text{C } (\text{m/s}) = 8.33 \times 10^{-30} (2.46 \times 10^{3} \ln S)^{6.7} \quad (31)$$

where W_{as} is the weight percent of antisolvent (H_2O), $S = c/c^*$ is the relative supersaturation, c and c^* are the solution and saturated concentration, respectively, and the coefficient 15.45763 in the temperature-dependence factor infers a heat of crystallization value of ΔH_{crys} = −38,042.5 kJ/kmol. The amount of heat released in this mixing of methanol and water (ΔH_{mix}) is a nonlinear function of the mass fraction of the solvent or antisolvent in the mixture. In order to account for that effect and simplify the implementation of ΔH_{mix} in the code, a polynomial function was fitted to the experimental data obtained by Bertrand et al.[29]

DOI: 10.1021/acs.iecr.8b01849
Ind. Eng. Chem. Res. 2018, 57, 11702−11711

The solubility and nucleation and growth rates were implemented in the software as external functions via PBESource.H and PBESource.C files. These functions are implemented in a single cell basis, which requires additional volScalarField variables to store the values and a loop over all the computational cells. This implementation is flexible and easier for the user to input any kind of explicit function for these terms.

The numerical solution was performed on 3D computational meshes. SolidWorks was used to generate the computer-aided design (CAD) model and to export every boundary as a STereoLithography (STL) file. The OpenFOAM mesh generation tool blockMesh was used to set up a basis mesh and the snappyHexMesh tool, with a proper dictionary, was applied to obtain a final hexahedral dominant mesh for every domain with around 290,000 cells, which corresponds to an average grid space between nodes of 0.001 m.

The population balance equation was discretized into 30 to 54 bins, as needed, for the longest growth axis, with $\Delta r = 8\ \mu$m. Transient simulations were run until the solutions achieved the steady-state.

5. RESULTS AND DISCUSSION

Figure 3 shows the volume fraction of methanol in the $YZ|_{x=0}$ symmetry plane for different crystallizers for a total mass flow rate of 0.264 kg/s. Unlike many previous works,[10,12−15] that either assumed averaged densities or ran the simulations in 2D with axial symmetry, this model/solver incorporates the effect of density variation, as seen by the asymmetry in the volume fraction profile in Figure 3. The dual impinging jet (Figure 3a) and radial mixers (Figure 3c) provide much better macromixing performance than the coaxial mixer (Figure 3b).

This behavior was also observed for the micromixing (Figure 4a). The dual impinging jet and radial mixers produce a higher turbulence dissipation rate (ε) than the coaxial mixer, resulting in better micromixing. The radial mixer produces the best micromixing, which can be due to a more symmetrical behavior, generated by the two antisolvent impinging jets fed in a 90° angle with the solvent stream farthest away from walls, and a higher turbulence intensity in the antisolvent feeding point.

Although the radial mixer had a better micromixing performance, the dual impinging jet achieved higher solute conversion for the same solution-antisolvent contact time (Figure 4f). At low contact time, the rapid increase in the volume fraction of the mixed environment (p_3) observed in the radial mixer increases the amount of heat released through the mixing process and, consequently, increases the temperature, as shown in Figure 4b. The higher the temperature, the lower the initial relative supersaturation (Figure 4c) and, consequently, the lower the initial nucleation and growth rates, Figures 4de, respectively. The temperature observed in the coaxial mixer was lower than the other geometries, and its poorer micromixing results in spatially delocalized nucleation and growth rates. These results show the importance of considering a complete energy balance and, more importantly, the heat of mixing in systems where this effect is significant.

Figure 5 shows the results for the mass-averaged full CSD calculated at the crystallizers' outlets. The narrower CSD observed for the radial mixer and broader CSD obtained for the dual impinging jet mixer are a result of a combination of the micromixing and heat of mixing effects, as well as the crystal nucleation and growth kinetics. The Sauter mean diameter (d_{32}) calculated for the dual impinging jet, coaxial, and radial

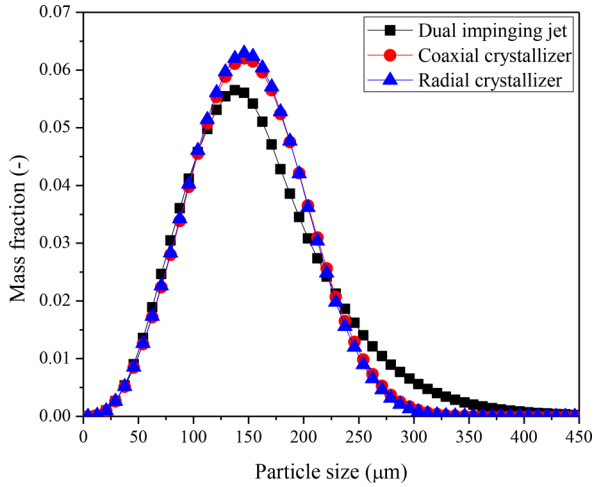

Figure 5. Mass-weighted average CSD calculated for a total mass flow rate of 0.264 kg/s at the axial position corresponding to a solute conversion of 70%.

crystallizers are 130, 128, and 120 μm, respectively. Due to the competing effects, the CSD is very similar for the best and worst performing mixers (radial and coaxial), and the broadest CSD occurs for the intermediate mixer (dual impinging jets).

The effects of increasing the mass flow rate, that is, the effect of the Reynolds number, on both macro- and micromixing are shown in Figures 6 and 7. As expected, increasing the mass

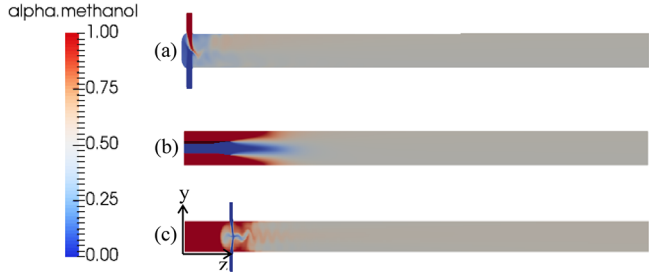

Figure 6. Volume fraction of methanol for a total mass flow rate of 1.06 kg/s: (a) dual impinging jet; (b) coaxial crystallizer; (c) radial crystallizer.

flow rate improved the macro- and micromixing for all of the mixers. The contact time required to achieve a volume fraction of the mixed environment equal to 0.90 was an average of 78% lower for the factor of 4 increase in total mass flow rate (cf. Figure 4a and 7a). The contact time was 33% lower to obtain a solute conversion of 70% (cf. Figure 4f and 7f).

As observed before, the radial mixer produced the best micromixing (Figure 7a). The better micromixing resulted in higher temperature values (Figure 7b), as explained before. At low contact time, the temperature difference between the radial and the other two mixers is as high as 6 K, which explains the low initial relative supersaturation (Figure 7c), crystal nucleation (Figure 7d), and growth (Figure 7e) observed for this crystallizer. As a consequence, the outlet solute conversion was the lowest (Figure 7f). On the other hand, the coaxial mixer poorer micromixing at low contact time (Figure 7a) causes its solute conversion to be much lower near the inlet than for the other geometries (Figure 7f). The lower temperature observed for the coaxial mixer after a contact time of 0.2 s makes its solute conversion rate to be greater at high contact time (Figures 7bf),

DOI: 10.1021/acs.iecr.8b01849
Ind. Eng. Chem. Res. 2018, 57, 11702−11711

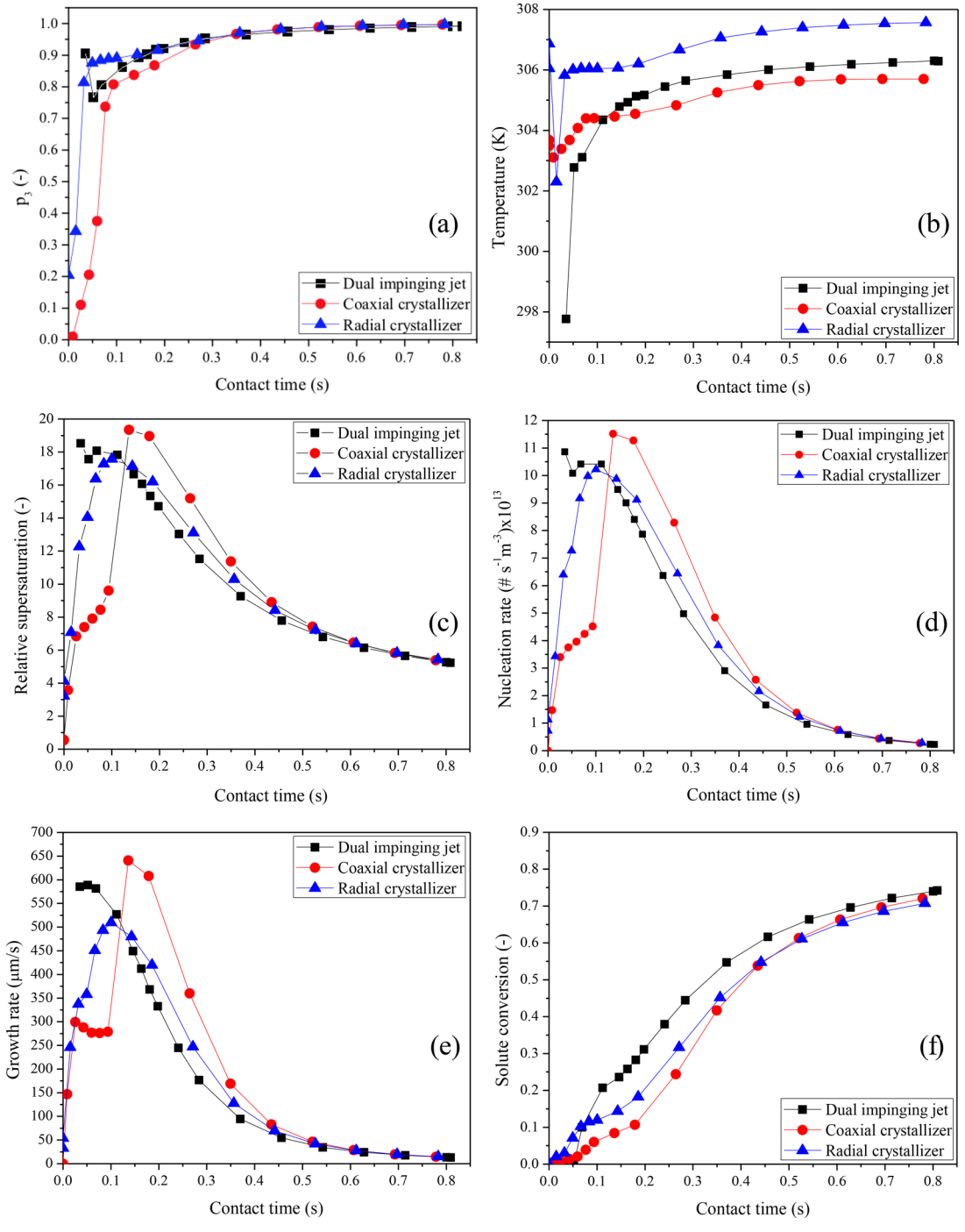

Figure 7. Mass-weighted average variables as a function of contact time calculated for a total mass flow rate of 1.06 kg/s: (a) volume fraction of the mixed environment; (b) temperature; (c) relative supersaturation; (d) nucleation rate; (e) growth rate; (f) solute conversion.

so that the outlet value is nearly the same as the other mixers. The dual impinging jet mixer showed a combination of sufficiently good micromixing and lower temperature at low contact time (Figure 7b), which resulted in the highest outlet solute conversion (Figure 7f).

The highest relative supersaturation and nucleation rate near the inlet occurs for the dual impinging jet mixer (Figure 7c), which gives the most time for the crystals to grow, resulting in the largest proportion of large crystals (Figure 8). The radial mixer, which generated lower relative supersaturation and nucleation and growth rates near the inlet, produced the narrowest CSD. The nucleation of crystals was delayed and so had less time to grow before reaching the outlet. Although the coaxial mixer had the lowest quality micromixing, its CSD was intermediate between the other two mixers. In other words, a narrower CSD can potentially be generated by making the mixing worse (compare dual impinging jet with coaxial) or by improving the mixing (compare coaxial with radial).

6. CONCLUSION

Open-source software was presented that couples a Reynolds-Averaged Navier−Stokes model with variable properties for macromixing with a multienvironment PDF model for micromixing, a spatially varying population balance equation, and

DOI: 10.1021/acs.iecr.8b01849
Ind. Eng. Chem. Res. 2018, 57, 11702−11711

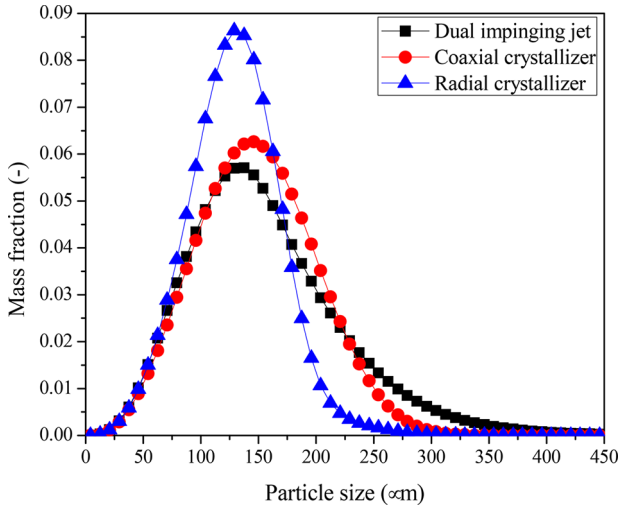

Figure 8. Mass-weighted average CSD calculated for a total mass flow rate of 1.06 kg/s at the axial position corresponding to a solute conversion of 70%.

energy balance and scalar transport equations. The OpenFOAM implementation enabled the simulation of combined antisolvent-cooling crystallization in different mixer geometries, providing in depth information on the micromixing behavior, the supersaturation driving force, the crystal growth and nucleation rates, and the full crystal size distribution. All of the simulations were numerically stable in our implementation.

The design of the crystallizer plays an important role in the micromixing and growth and nucleation rates, and consequently in the solute conversion and crystal size distribution. As expected, a narrower CSD and smaller particles were produced when the crystallizers were operated with higher total mass flow rates. Other simulation results were less expected. The simulation results indicated that the heat of mixing is an important effect to be considered in the energy balance for the studied system. While the radial crystallizer provided better micromixing, the dual impinging jet had superior solute conversion. This behavior was attributed to higher temperature values achieved in the radial crystallizer, which reduced the supersaturation and, consequently, the growth and nucleation rates. In other words, it is possible for the CSD to become narrower by making the mixing worse or better. The complex interplay of crystallizer kinetics and momentum, mass, and heat transfer makes the selection of the best mixer for a particular application to be nonobvious, which motivates the development and application of high-fidelity multiscale simulations for the design of antisolvent crystallizers.

■ ASSOCIATED CONTENT

Supporting Information

The Supporting Information is available free of charge on the ACS Publications website at DOI: 10.1021/acs.iecr.8b01849.

OpenFOAM implementation of the probability transport equation, semidiscrete PBEs, and energy balance. (PDF)

■ AUTHOR INFORMATION

Corresponding Author

*E-mail: darosacezar@gmail.com; phone: 55-53-3293-5370.

ORCID

Cezar A. da Rosa: 0000-0003-2164-5943

Richard D. Braatz: 0000-0003-4304-3484

Notes

The authors declare no competing financial interest.

■ NOMENCLATURE

B	Nucleation rate [#/m^3·s]
c	Concentration of solute [kg/m^3 or kg/kg]
c^*	Solubility or saturation concentration [kg/m^3 or kg/kg]
Δc	Supersaturation [kg/m^3 or kg/kg]
D, D_m	Diffusion coefficient or laminar diffusivity [m^2/s]
D_t	Turbulent diffusivity [m^2/s]
f	Number density function [#/m$_c$·m^3]
f_r	Derivative of number density function [#/m$_c^2$·m^3]
f_w	Mass density function [kg/m$_c$·m^3]
f_ϕ	Joint probability function of all scalars
$\vec{g}$	Gravitational acceleration [m/s^2]
G	Growth rate [m/s]
$\mathbf{G}(\mathbf{p})$	Rate of change of $\boldsymbol{p}$ = [p_1 p_2 ... p_{Ne}] due to micromixing
$\mathbf{G_s}(\mathbf{p})$	Term to eliminate spurious dissipation rate in eq [12]
h	enthalpy per unit mass, J/kg
k	Turbulent kinetic energy [m^2/s^2] in turbulence and micromixing equations Boltzmann's constant in nucleation rate expression
k_v	Volume shape factor
$\mathbf{M}^n$	Rate of change of $\langle \mathbf{s} \rangle_n$ due to micromixing
$\mathbf{M}_s^n$	Term to eliminate spurious dissipation rate in eq [13]
N	Number of particle size cells or bins
N_e	Number of probability modes or environments
p	Pressure [Pa] in momentum conservation equation
p_n	Probability of mode n or volume fraction of environment n in micromixing model
r	Crystal size [m]
r_0	Nuclei size [m]
Δr	Discretized bin size for crystal size [m]
Re	Reynolds number
$\langle \mathbf{s} \rangle_n$	Weighted concentration of mean composition of scalars ϕ in mode n
S	Relative supersaturation = c/c^*
S_{as}	User-defined source term of antisolvent concentration [kg/m^3·s]
S_ε	User-defined source term for dissipation rate of turbulent kinetic energy
S_k	User-defined source term for turbulent kinetic energy
t	Time [s]
T	Temperature [°C]
$\vec{v}$	Velocity vector [m/s]
W_{as}	Antisolvent mass percent [%]

Special units

m	Length unit (meter) in mixer/crystallizer
m$_c$	Length unit (meter) in crystal
m$_3$	Length unit (meter) in environment 3

Symbols

Δc	supersaturation = $c - c^*$
ε	Turbulent kinetic energy dissipation rate [m^2/s^3]
ε_ξ	Scalar dissipation rate [1/s]
φ	Volume fraction of solids in effective viscosity expression
φ_k	Scalar
$\langle \phi \rangle$	Mean composition of scalar in environment
ρ_3	Fluid density of Environment 3
μ	Viscosity [kg/m·s] Effective viscosity of suspension [kg/m·s] in effective viscosity expression
μ_t	Turbulent viscosity [kg/m·s]
θ	Constant in minmod limiter

DOI: 10.1021/acs.iecr.8b01849
Ind. Eng. Chem. Res. 2018, 57, 11702−11711

ρ Density [kg/m^3]
ρ_c Crystal density [kg/m^3]
τ Stress tensor [kg/m·s^2]
ν Kinematic viscosity [m^2/s]
$\langle\xi\rangle$ Mixture fraction
$\langle\xi'^2\rangle$ Mixture fraction variance

Subscripts

i Crystal dimension in the population balance equation instance for dropping seed crystals
c Crystal property
j Discretized bin for crystal size in population balance equation
n Environment in micromixing model

REFERENCES

(1) McCabe, W. L.; Smith, J. C.; Harriot, P. *Unit Operations of Chemical Engineering*, 7th ed.; McGraw-Hill: New York, 2004.
(2) Nowee, S. M.; Abbas, A.; Romagnoli, J. A. Model-Based Optimal Strategies for Contolling Particle Size in Antisolvent Crystallization Operation. *Cryst. Growth Des.* **2008**, *8*, 2698.
(3) Mullin, J. W. *Crystallization*; Elsevier Butterworth-Heineman: Oxford, 2001.
(4) Wey, J. S.; Karpinski, P. H. Batch Crystallization. In *Handbook of Industrial Crystallization*; Myerson, A. S., Eds.; Butterworth-Heinemann: Boston, 2002; pp 231−248.
(5) Jiang, M.; Li, Y. D.; Tung, H.; Braatz, R. D. Effect of Jet Velocity on Crystal Size Distribution from Antisolvent and Cooling Crystallizations in a Dual Impinging Jet Mixer. *Chem. Eng. Process.* **2015**, *97*, 242.
(6) Schall, J. M.; Mandur, J. S.; Braatz, R. D.; Myerson, A. S. Nucleation and Growth Kinetics for Combined Cooling and Antisolvent Crystallization in an MSMPR System: Estimating Solvent Dependency. *Cryst. Growth Des.* **2018**, *18*, 1560.
(7) Rahimi, M.; Akbari, M.; Parsamoghadam, M. A.; Alsairafi, A. A. CFD Study on Effect of Channel Confluence Angle on Fluid Flow Pattern in Asymmetrical Shaped Microchannels. *Comput. Chem. Eng.* **2015**, *73*, 172.
(8) Qian, F.; Huang, N.; Lu, J.; Han, Y. CFD−DEM Simulation of the Filtration Performance for Fibrous Media Based on the Mimic Structure. *Comput. Chem. Eng.* **2014**, *71*, 478.
(9) Lee, Y. R.; Choi, H. S.; Park, H. C.; Lee, J. E. A Numerical Study on Biomass Fast Pyrolysis Process: A Comparison Between Full Lumped Modeling and Hybrid Modeling Combined with CFD. *Comput. Chem. Eng.* **2015**, *82*, 202.
(10) Woo, X. Y.; Tan, R. B. H.; Chow, P. S.; Braatz, R. D. Simulation of Mixing Effects in Antisolvent Crystallization Using a Coupled CFD-PDF-PBE Approach. *Cryst. Growth Des.* **2006**, *6*, 1291.
(11) Woo, X. Y.; Tan, R. B. H.; Braatz, R. D. Modeling and Computational Fluid Dynamics-Population Balance Equation-Micromixing Simulation of Impinging Jet Crystallizers. *Cryst. Growth Des.* **2009**, *9*, 156.
(12) Pirkle, J. C., Jr.; Foguth, L. C.; Brenek, S. J.; Girard, K.; Braatz, R. D. Computational Fluid Dynamics Modeling of Mixing Effects for Crystallization in Coaxial Nozzles. *Chem. Eng. Process.* **2015**, *97*, 213.
(13) Marchisio, D. L.; Barresi, A. A.; Fox, R. O. Simulation of Turbulent Precipitation in a Semi-Batch Taylor-Couette Reactor Using CFD. *AIChE J.* **2001**, *47*, 664.
(14) Marchisio, D. L.; Fox, R. O.; Barresi, A. A.; Baldi, G. On the Comparison Between Presumed and Full PDF Methods for Turbulent Precipitation. *Ind. Eng. Chem. Res.* **2001**, *40*, 5132.
(15) Marcfflsio, D. L.; Fox, R. O.; Barresi, A. A.; Baldi, G. On the Simulation of Turbulent Precipitation in a Tubular Reactor via Computational Fluid Dynamics (CFD). *Trans IChemE* **2001**, *79*, 998.
(16) Silva, L. F. L. R.; Lage, P. L. C. Development and Implementation of a Polydispersed Multiphase Flow Model in OpenFOAM. *Comput. Chem. Eng.* **2011**, *35*, 2653.
(17) Holmes, L.; Favero, J.; Osswald, T. Numerical Simulation of Three-Dimensional Viscoelastic Planar Contraction Flow Using the Software OpenFOAM. *Comput. Chem. Eng.* **2012**, *37*, 64.
(18) Liu, Y.; Hinrichsen, O. CFD Modeling of Bubbling Fluidized Beds Using OpenFOAM®: Model Validation and Comparison of TVD Differencing Schemes. *Comput. Chem. Eng.* **2014**, *69*, 75.
(19) Cheng, J. C.; Yang, C.; Jiang, M.; Li, Q.; Mao, Z. S. Simulation of Antisolvent Crystallization in Impinging Jets with Coupled Multiphase Flow-Micromixing-PBE. *Chem. Eng. Sci.* **2017**, *171*, 500.
(20) da Rosa, C. A.; Braatz, R. D. Multiscale Modeling and Simulation of Macromixing, Micromixing, and Crystal Size Distribution in Radial Mixers/Crystallizers. *Ind. Eng. Chem. Res.* **2018**, *57*, 5433.
(21) Fox, R. O. *Computational Models for Turbulent Reacting Flows*; Cambridge University Press: Cambridge, 2003.
(22) Wang, L.; Fox, R. O. Comparison of Micromixing Models for CFD Simulation of Nanoparticle Formation. *AIChE J.* **2004**, *50*, 2217.
(23) Randolph, A. D.; Larson, M. A. *Theory of Particulate Processes*; Academic Press, Inc.: San Diego, 1988.
(24) Kurganov, A.; Tadmor, E. New High-Resolution Central Schemes for Nonlinear Conservation Laws and Convection-Diffusion Equations. *J. Comput. Phys.* **2000**, *160*, 241.
(25) Versteeg, H. K.; Malalasekera, W. *An Introduction to Computational Fluid Dynamics: The Finite Vol. Method*; Longman Scientific & Technical: Harlow, 1995.
(26) Jasak, H. Error Analysis and Estimation for the Finite Volume Method with Applications to Fluid Flows. Ph.D. Dissertation, Imperial College of Science, Technology and Medicine, London, UK, 1996.
(27) Passalacqua, A.; Fox, R. O. Implementation of an Iterative Solution Procedure for Multi-Fluid Gas−Particle Flow Models on Unstructured Grids. *Powder Technol.* **2011**, *213*, 174.
(28) Mahajan, A. J.; Kirwan, D. J. Nucleation and Growth Kinetics of Biochemicals Measured at High Supersaturations. *J. Cryst. Growth* **1994**, *144*, 281.
(29) Bertrand, G. L.; Millero, F. J.; Wu, C.-H.; Hepler, L. G. Thermochemical Investigations of the Water-Ethanol and Water-Methanol Solvent Systems. I. Heats of Mixing, Heats of Solution, and Heats of Ionization of Water. *J. Phys. Chem.* **1966**, *70*, 699.

DOI: 10.1021/acs.iecr.8b01849
Ind. Eng. Chem. Res. 2018, 57, 11702−11711